

Scalability of gadolinium-doped-water Cherenkov detectors for nuclear nonproliferation

Viacheslav A. Li,^{*} Steven A. Dazeley, Marc Bergevin, and Adam Bernstein

Lawrence Livermore National Laboratory, Livermore, CA 94550

(Dated: April 18, 2022)

Antineutrinos are an unavoidable byproduct of the fission process. The kiloton-scale KamLAND experiment has demonstrated the capability to detect reactor antineutrinos at few-hundred-km range. But to detect or rule out the existence of a single small reactor over many km requires a large detector. So large in fact that the optical opacity of the detection medium itself becomes an important factor. If the detector is so large that photons cannot traverse across the detector medium to an optical detector, then it becomes impractical. For this reason, gadolinium-doped-water Cherenkov detectors have been proposed for large volumes, due to their appealing light-attenuation properties. Even though Cherenkov emission does not produce many photons and the energy resolution is poor, there may be a place for Gd-doped-water detectors in the far-field nuclear reactor monitoring. In this paper, we focus on the reactor discovery potential of large-volume Gd-doped-water Cherenkov detectors for nuclear nonproliferation applications. Realistic background models for the worldwide reactor flux, geo-neutrinos, cosmogenic fast neutrons, and detector-associated backgrounds are included. We calculate the detector run time required to detect a small 50-MWt reactor at a variety of stand-off distances as a function of detector size. We highlight that at present, PMT dark rate and event reconstruction algorithms are the limiting factors to extending beyond ~ 50 -kt fiducial mass.

INTRODUCTION

Nuclear reactors produce enormous numbers of antineutrinos as a consequence of the production of beta-decaying neutron-heavy fission daughters. In fact, a typical large nuclear power reactor (~ 1 GWt) generates more than $\sim 10^{19}$ fissions per second and $\sim 10^{20}$ antineutrinos per second during normal operation. Each fissioning isotope produces its own spectrum of daughter isotopes. Therefore, the resulting antineutrino flux and energy spectrum is sensitive to the fuel content [1]. Furthermore, since antineutrinos only interact weakly with matter, they are impossible to shield [2]. Therefore, information about the operational status and fuel content of a reactor can in principle be monitored remotely at significant distances via the antineutrino flux.

Although growth in the worldwide number of reactors since the mid 1980s has been slow, about 500 nuclear power reactors world-wide currently account for $\sim 10\%$ of global electricity production. Despite being a carbon-free energy source, one of the reasons for the slow nuclear growth rate is the enormous capital cost of building a new nuclear reactor. Future reactor designs address this issue by attempting to go smaller and simpler. Small Modular Reactors (SMRs), are designed to be simpler to operate and reduce capital costs [3]. Some new reactor designs utilize smaller fuel elements, or liquid fuel. These designs may be more difficult to safeguard using present-day techniques which emphasize item accountancy.

Recently, methods for monitoring the operational status of future reactor designs have been proposed that don't rely on item accountancy. One such method is to monitor the antineutrino emissions of these reactors.

The reality is however, that antineutrinos are extremely difficult to detect for the same reasons they are impossible to shield [4]. The range over which it is practical to monitor a reactor will be limited by cost considerations related to detector size and the requirement to place such detectors underground to shield from cosmic-ray-induced backgrounds.

In recent years, reactor antineutrino detectors have been deployed at 1–2 km distances to measure neutrino-oscillation properties [5–9], and a 1-kiloton detector called KamLAND, was situated at a flux weighted average distance of ~ 180 km from Japan's reactor fleet to study oscillation at long range [10]. In the very near future, the JUNO detector will commence operations at a distance of 53 km from two reactor complexes in China [11]; while the SNO+ detector — in Canada, will be able to observe several CANDU reactors with an effective baseline of a couple of hundred kilometers [12]. All of these experiments use liquid organic scintillator as the detection medium. The fundamental limit to the size of these detectors is the attenuation of light, which is ~ 10 –20 m in liquid scintillator.

Gd-doped water is another medium for reactor-antineutrino detection, which makes use of Cherenkov light instead of scintillation light. One existing example is Super-Kamiokande [13], which has completed an initial fill of Gd-H₂O using gadolinium sulfate octahydrate at approximately one tenth of the goal concentration of 0.2% by mass. While Cherenkov emission produces less light with poorer energy resolution, attenuation lengths approaching ~ 100 m are achievable with Gd-doped water, which might enable very large detectors [14].

In 2015, the WATCHMAN collaboration proposed to

demonstrate monitoring of a single reactor site using the Hartlepool reactor, with a detector to be deployed 26 kilometers away in the Boulby mine [15]. Planning for this effort ceased following a UK government announcement in 2021 of premature shutdowns of the Hartlepool and other reactors, which would have compromised the deployment schedule for the Boulby site.

Gadolinium-doped water is sensitive to electron antineutrinos via the inverse beta decay (IBD) reaction:

$$\bar{\nu}_e + {}^1\text{H} \rightarrow e^+ + n \quad (1)$$

For reactor antineutrinos, the prompt (e^+) is few MeV. The Cherenkov light from the positron (few MeV) is detectable, however the 511-keV gammas do not deposit a sufficient energy to generate Cherenkov light [16, 17]. The neutron captures primarily on ${}^{155}\text{Gd}$ or ${}^{157}\text{Gd}$, producing a few gamma rays of few-MeV each [18, 19], which sum to 8 MeV. The gammas then Compton-scatter, producing sufficient Cherenkov light to permit detection of a delayed event. The average delay between the positron flash and the thermal-neutron capture depends on the concentration of gadolinium in the water. At 0.1%, the neutron capture time is $\sim 30 \mu\text{s}$.

To collect the Cherenkov photons, the detector requires a sufficiently high coverage of photosensors. In the Super-Kamiokande, about 40% of the detector wall area is effectively covered with photomultiplier tubes. Light attenuation is on the order of a few hundred meters [20, 21] at the blue wavelength suitable for PMT detection in large detector volumes. At few MeV energies, only a handful of photo electrons are produced. So, in addition to high photocathode coverage of the detector, a high quantum efficiency, low radioactivity, and low dark noise are desired characteristics of the PMTs.

For nonproliferation and science alike, Gd-doped water may be a cost-efficient and environmentally-friendly alternative compared to liquid-scintillator based detectors. In the early 2000s, there were several proposals to dope water Cherenkov detectors with gadolinium in order to be sensitive to the inverse-beta-decay reaction [22, 23]. Since then many projects have been pursued to study the feasibility of the technique, summarized in Table I. Measurements of the effect of Gd doping on water transparency have been performed with EGADS [14], the largest engineering/physics demonstration to date.

The number of IBD interactions inside a detector located at some distance from a reactor source can be calculated as follows. Each fission results in ~ 6 antineutrinos on average. Approximately a quarter of these are above the IBD 1.8-MeV threshold. Since the antineutrinos are emitted isotropically, the IBD interaction rate can be es-

Project	Mass [tons]	Gd content	Ref.
Watanabe et al.	0.002	0.2% wt. GdCl_3	[24]
WAND	1.0	0.4% wt. GdCl_3	[25]
ANGRA	1.3	0.2% wt. GdCl_3	[26]
WATCHBOY	2	0.2% wt. GdCl_3	[27]
ANNIE	26	0.2% wt. $\text{Gd}_2(\text{SO}_4)_3$	[28]
EGADS	200	0.2% wt. $\text{Gd}_2(\text{SO}_4)_3$	[14]
WATCHMAN	6,000 [1,000]	0.2% wt. $\text{Gd}_2(\text{SO}_4)_3$	[15]
SuperK-Gd	50e3 [22.5e3]	0.2% wt. $\text{Gd}_2(\text{SO}_4)_3$	[13]

TABLE I. Global research efforts on Gd-H₂O technology. Gadolinium is added in the form of either gadolinium chloride or sulfate, and has natural isotopic abundances (no isotopic enrichment). For WATCHMAN and SuperK, a corresponding fiducial mass is also listed in square parentheses.

timated as:

$$N_{IBD} \cong 1.5 P_{surv} \times \left(\frac{\text{power}}{50 \text{ MWth}} \right) \times \left(\frac{\text{mass}}{10 \text{ kt}} \right) \times \left(\frac{\text{time}}{1 \text{ day}} \right) \times \left(\frac{\text{distance}}{10 \text{ km}} \right)^{-2} \quad (2)$$

where P_{surv} is a probability of electron antineutrino to retain its flavor — the so-called survival probability. It is important to note that the survival probability is a function of antineutrino energy and distance. Survival probability factor P_{surv} , due to neutrino oscillations, can contribute up to a factor of few suppression, depending on the energy and stand-off distance. For example, the effect of oscillations is especially pronounced for 5-MeV antineutrino at ~ 100 -km distance, as shown in Fig. 1.

As shown by [31], for the purposes of nuclear nonproliferation, even a relatively small reactor of 50 MW thermal power is capable of producing a significant quantity of plutonium (8 kg) in one year. With the assumptions of 100% detection efficiency and zero detector background, the study provided estimates of the time required to detect such a reactor under various world-reactor-background conditions. By contrast, this paper takes into account more realistic efficiency estimates and detector related backgrounds; thus, the dwell times obtained are longer, but might be considered more realistic. To account for the sometimes large variations in the world-wide reactor-antineutrino background, the same three test locations are assumed here: Andes, Baksan, and Frejus. The closest power reactor at the Andes location is 563 km away, at Baksan — it is 360-km distant, and at Frejus — 133 km. The world-reactor background varies by approximately a factor of 100 between Low, Medium, and High test locations, as listed in Table II.

Fig. 2 shows the antineutrino flux spectrum, the IBD interaction cross section, and the IBD interaction spectrum that can be expected from a hypothetical 50-MWt test reactor located at a distance of 20 km from a hypothetical detector. The antineutrino spectrum from our test reactor is calculated based on the reactor power, fuel

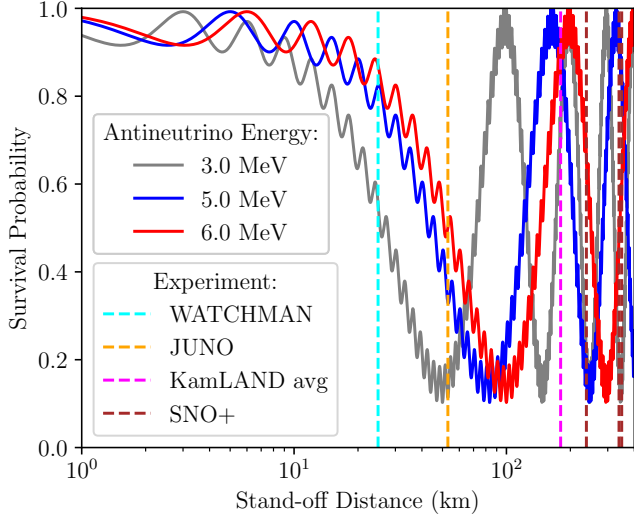


FIG. 1. Survival probability of electron antineutrinos as a function of distance, with a number of far-field detector baselines shown (for KamLAND, a flux-weighted average baseline is plotted). Antineutrinos with energies higher than about 4 MeV become visible in a water-Cherenkov detector. These are significantly suppressed at ~ 50 – 100 -km distances (the “death valley” for reactor antineutrinos).

content, and distance to the detector. Neutrino oscillations become a significant factor in the far-field. Fig. 3 shows the antineutrino spectrum normalized by $1/L^2$, and folded with antineutrino survival probability. Note that the antineutrino fluxes for 100-km and 200-km baselines are comparable above 5-MeV antineutrino energy due primarily to the effect of oscillations. The low-energy antineutrinos are impacted by the detector threshold effects in large water-Cherenkov detectors. This detector threshold effect is illustrated in Fig. 3, and will be further detailed in the next section.

To obtain IBD event rates in a realistic detector, we implement an algorithm approximated by the formula:

$$R_d = \left(\int R_e \sigma_{IBD} P_{surv} \frac{1}{4\pi L^2} \epsilon_+ dE_+ \right) \epsilon_n N_t f_{2m} f_{100\mu s} \quad (3)$$

where R_d is the IBD detected rate; R_e — the emitted antineutrino spectrum (taking into account reactor power and fuel composition); σ_{IBD} — the IBD cross-section (a function of energy); P_{surv} — antineutrino survival probability (a function of energy and distance); L — distance between the reactor and the detector; ϵ_+ — positron detection efficiency (a function of energy); E_+ — positron energy; ϵ_n — neutron detection efficiency; N_t — number of targets (hydrogen nuclei) in the fiducial volume; f_{2m} — 2-meter spacial proximity coefficient (in the range of 91%–98%); and $f_{100\mu s}$ — 100-microsecond temporal proximity coefficient (set at 98%). The fuel composition

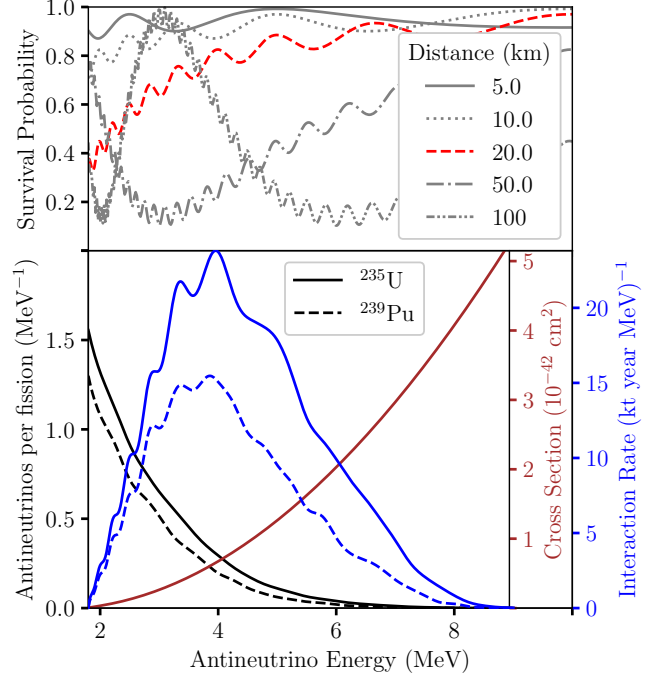


FIG. 2. An antineutrino spectrum at the detector location would have a form shown in blue lines, which takes into account an emitted spectrum, fission energy per isotope, antineutrino survival probability, and the IBD cross-section. The full Strumia-Vissani approximation for the IBD cross-section [29] and Huber model for the emitted reactor spectrum [30] are shown. An IBD interaction rate in a kiloton water detector from 50-MWt reactor at 20-km stand-off distance with a two hypothetical cores — 100% ^{239}Pu fission fractions (dashed blue line) and 100% ^{235}U fission fractions (solid blue line); a realistic core would lie in between these two curves. *Top panel*: survival probability of reactor antineutrinos as a function of antineutrino energy for selected stand-off distances; the 20-km curve, highlighted in red, is folded to get the interaction rate shown in the bottom plot (blue curves).

Background	Total rate	CR rate	CR distance
Low	6.6	1.6	563 km
Medium	65.4	2.5	360 km
High	798.7	64.3	133 km

TABLE II. Total world-reactor background rates, in units of IBD interactions per kiloton of water per year, for three representative locations that have a High, Medium, and Low reactor-antineutrino flux. Closest reactor (CR) rate and distance are also listed for each location.

is kept constant in this study, and is listed in Table III.

DETECTOR DESCRIPTION

In the following, we investigate the sensitivity of large water Cherenkov detectors doped with gadolinium. We are interested in estimating the detector size required to

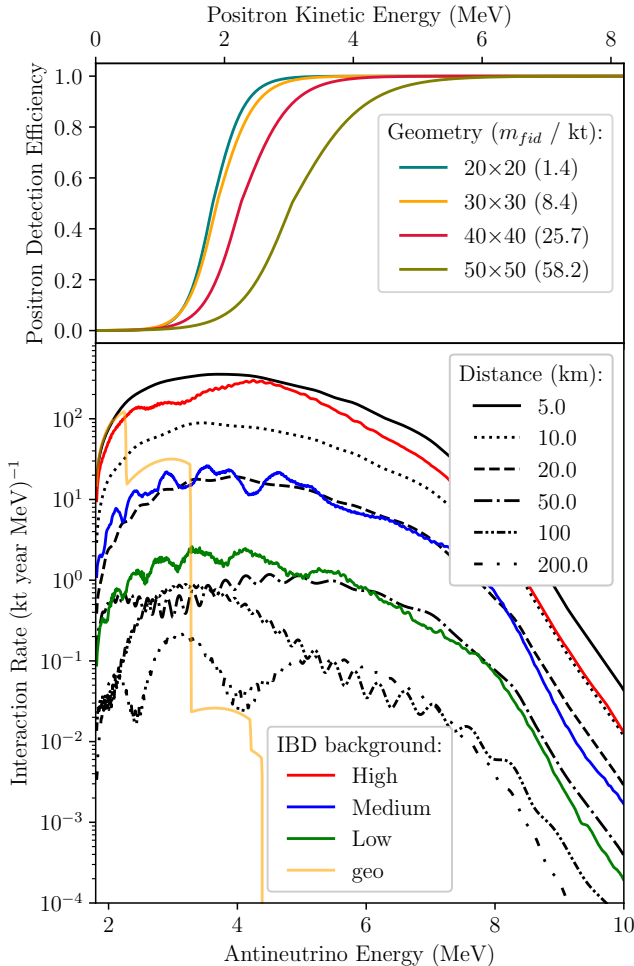


FIG. 3. IBD interaction rate as a function of antineutrino energy for three locations. For reactor the power is set at 50 MWt and the fuel composition is PWR, using Huber model for the emitted reactor spectrum. Each of the positron detection efficiency curves shown (on the top plot) were generated assuming a minimum number of PMT hits. The PMT hit threshold can be optimized for different detector sizes. The details of this optimization are presented in the next section. The geo-neutrinos are invisible in water-Cherenkov detectors (for geo-neutrinos a location at Frejus is shown as an example).

	^{235}U	^{238}U	^{239}Pu	^{241}Pu
Fission fraction	0.56	0.08	0.30	0.06
Energy / fission [MeV]	201.9	205.0	210.9	213.4

TABLE III. Fuel composition (fission fractions) and energy release per fission used in this study.

successfully detect within one year a test reactor at various distances. In all cases, the assumed detector is a right cylinder shape (like Super-K), with photocoverage is fixed at 40%. The veto thickness (to suppress cosmogenic spallation neutrons from the surrounding rock) is fixed at 2 meters. The inner detector is also a right

cylinder. The PMTs are modeled on 10-inch Hamamatsu 7081 PMTs equipped with low-activity glass. An average dark rate of 3 kHz per PMT is also assumed, based on internal measurements of a selection of about a hundred PMTs. All inward facing PMTs are placed perpendicular to the wall. The fiducial volume boundary is placed at 2 meters from the PMT wall to reduce PMT-based radiation background.

Event position reconstruction is done using a software package adapted from Super-K called BONSAI [32]. For a given event energy, the detector response depends somewhat on the event position. However for small detectors, the detector response over the fiducial volume is approximately constant. For large detectors, light attenuation can become significant, so the response of events in the center of the detector is generally slightly smaller than the response near the edge of the fiducial volume. Nevertheless, for this work we have used the approximation that the number of detected photons detected within a Cherenkov wavefront is proportional to the energy of a (minimum ionizing) particle. To count Cherenkov photons, the time residuals of the position reconstructions are used: n_9 is the number of PMTs with time residuals between -3 ns and $+6$ ns (values are chosen based on PMT timing uncertainty and expected light scattering). In the following, n_9 will serve as a rough energy estimator. The “ n_9 ” parameter is modeled after a similar parameter used at Super-K [33, 34], using a larger time range (18 nanoseconds). The smaller time window was considered appropriate for this study due to the improved time resolution of the Hamamatsu 10” PMTs. A set of detector geometries of between 0.3 kt and 58 kt fiducial were studied here, and listed in Table IV.

d [m] × h [m]	m [kt]	m_f [kt]	# of 10” PMTs
15×15	2.7	0.3	4512
20×20	6.2	1.4	9516
30×30	21.2	8.4	25182
40×40	50.3	25.7	48258
50×50	98.2	58.2	78856

TABLE IV. Simulated detector geometries. The fiducial volume is defines as 4 meters from the outer tank, or 2 meters from the PMTs. Other geometries are being interpolated based on the simulated ones.

A GEANT4-based simulation package called RAT-PAC [35] is used throughout this study. While based on GEANT4 [36], it includes useful features specifically designed for reactor-antineutrino detector simulations. It was recently further adapted by the WATCHMAN collaboration [15]. A visualization of a 50×50 geometry is shown in Fig. 4.

Physics events in the few MeV region only produce a few dozen photoelectrons. Most PMTs register only one photoelectron. Fig. 5 shows the relation between the n_9 parameter and the true positron energy, as simulated in

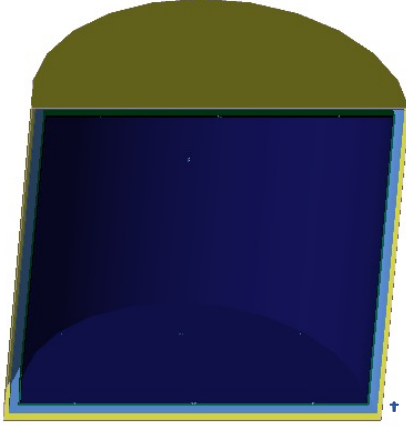


FIG. 4. GEANT4 (RAT-PAC) visualization of one of the detector geometries. The distance (outer veto region) between the inner tank and the outer tank is kept at 2 meters in all simulations. In this particular view, a cutaway of the 50×50 geometry is presented with only a few 10-inch PMTs (those little dots on the image) to demonstrate the scale. A figure of a person is shown approximately to-scale.

RAT-PAC, along with a plot of energy resolution versus the energy.

Geometry	$n9_{pr}$	$n9_{del}$	2-m fraction	f_{2m}	$f_{100\mu s}$
15×15	17	25	0.05256	99%	98%
20×20	17	25	0.02469	99%	98%
30×30	18	25	0.00401	97%	98%
40×40	20	25	0.00130	94%	98%
50×50	26	26	0.00058	91%	98%

TABLE V. Prompt $n9$ cuts obtained using optimization for four different detector sizes, as well as 2-meter bubble fractions used in estimation of IBD-like accidental backgrounds. The IBD spatial and temporal proximity coefficients are also listed, as used in IBD signal and background calculations.

IBD event candidates were selected on the basis of characteristics: 1) prompt signal; 2) delayed signal; 3) the position in the detector; 4) the time and distance between correlated pairs. A summary of the analysis cuts used are presented in Table V. In order to simplify the analysis, and aid in scaling sensitivity between each of the simulated detector sizes, it was decided to fix some of the analysis cuts *a priori*. For example, the fiducial volume was defined to extend to 4 m from the tank wall for all detector sizes. The maximum distance and time between correlated event pairs were defined to be 2 m and 100 μs respectively. These initial guesses were informed by an initial round of simulations which indicated limited sensitivity to detector size. The remaining analysis cuts, the $n9$ prompt and delayed, are somewhat dependent on the detector size. However, in the interests of simplicity, since the $n9$ prompt cut was found to be the most sensitive to detector performance, we opted to optimize only

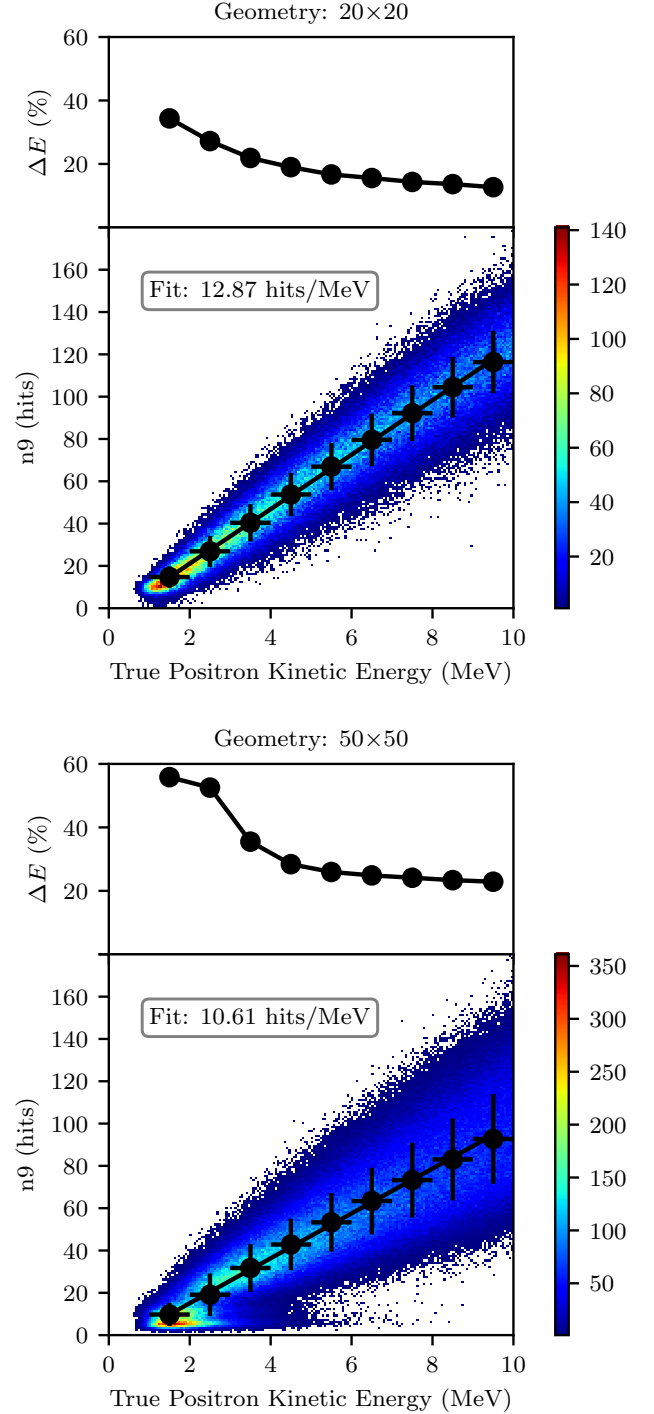


FIG. 5. The reconstructed number of PMT hits within 9-nanosecond window ($n9$ parameter) versus positron kinetic energy (Monte Carlo true) for a flat $[0, 10]$ -MeV positron spectrum in the fiducial volume. A detector trigger threshold of 10 PMT hits was applied. *Top panel:* 20×20 geometry; *bottom:* 50×50 . The comparison shows that a degradation in energy resolution ΔE accompanies increased detector sizes. The large number of events in the bottom left corner of the plot for the 50×50 geometry indicates mis-reconstruction of low-energy events.

n9 prompt, while setting the n9 delayed to a reasonable constant value (where possible). An optimization of the n9 prompt analysis cut was performed for each detector size (using detector dwell time as the metric), maintaining all the other analysis cuts constant, shown in Fig. 6. The primary detector background that impacts the n9 prompt cut optimization originates from radioactive decays in the PMT glass and the detection medium. The central regions of the detector medium can be expected to be relatively radio-pure [37]. Our simulations assumed levels of trace radioactive nuclei in the water consistent with Super-K. This resulted in a low level (but still significant) background event rate. The primary source of background events was due to the ^{238}U and ^{232}Th decay chains. The most problematic isotopes were ^{214}Bi , ^{212}Bi , and ^{208}Tl .

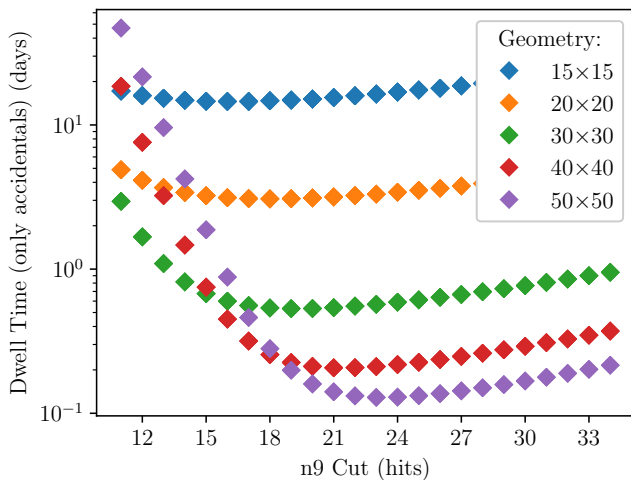


FIG. 6. The dwell-time metric based on Eq. 9 including only detector accidental backgrounds to estimate optimal n9 cut on the prompt (minimum of these curves). For the 50×50 geometry, an optimal n9 cut was chosen 26 to eliminate the effect of the PMT dark rate.

Detection efficiency

As mentioned previously, five distinct detector sizes were simulated. To determine the performance of intermediate detector sizes, a series of interpolations were used. The first step in this process was to generate a set of efficiency curves for positrons and neutrons. For each configuration in Table IV, positrons were simulated with a flat spectrum $[0, 10]$ -MeV distributed uniformly in the detector fiducial volume. A set of efficiency curves was then generated and parametrized using a combination of two Fermi functions:

$$\epsilon = \frac{1}{2} \left[\frac{1 + \text{sign}(E - b)}{1 + \exp(-a_0(E - b))} + \frac{1 + \text{sign}(-E + b)}{1 + \exp(-a_1(E - b))} \right] \quad (4)$$

where E is the positron kinetic energy and “sign” is a sign function, such as $\text{sign}(x) = \pm 1$ if $x \gtrless 0$. For each n9-parameter cut and each *simulated* geometry, we obtained efficiency curves and a set of stored fit parameters a_0 , a_1 , and b in a lookup table. The b coefficient is the energy at 50% efficiency. A set of positron efficiency curves are shown in Fig. 7 for an n9 cut of 26 PEs. The positron efficiency curves shown in Fig. 3 were generated using the optimized n9 thresholds presented in Table V.

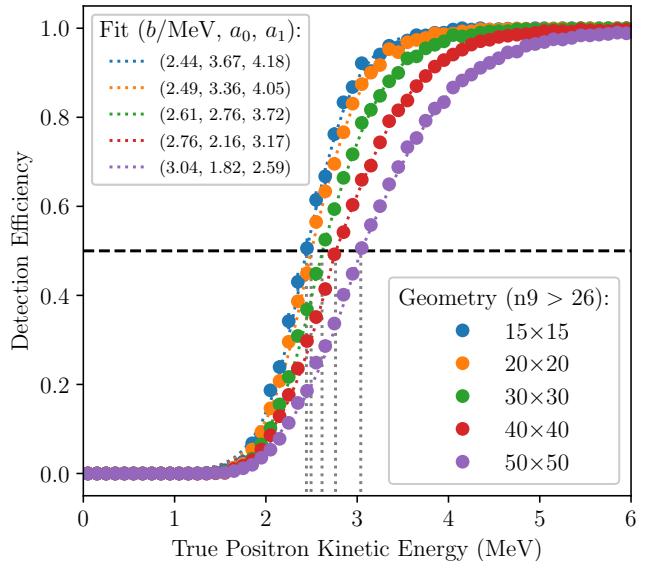


FIG. 7. Positron detection efficiency as a function of Monte Carlo positron kinetic energy. Efficiency curves for $n9 > 26$ are shown as an example here. The vertical dashed lines correspond to the energies at 50% efficiency level — the b parameter in the fit.

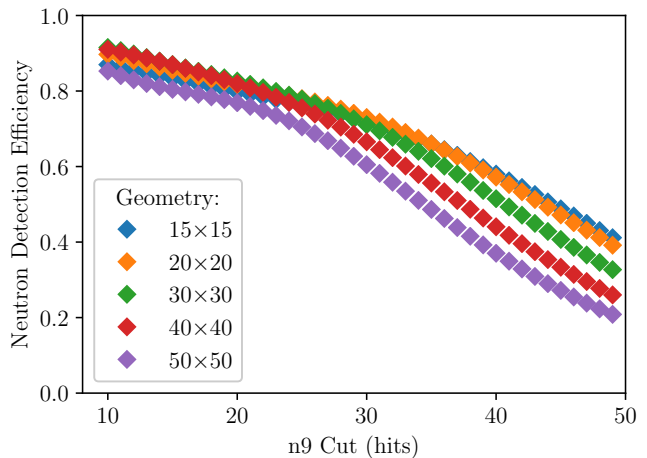


FIG. 8. Neutron detection efficiency as a function of n9 cut and detector size (the fiducial cut is applied).

Detected signal and background events

One source of IBD-like backgrounds are accidental coincidences of gamma-rays and neutrons generated by radioactive decays occurring in detector materials. These consist of two categories:

- Volume — originate due to radioactive contaminants in the water (Rn/U/Th/K)
- Surface — originate from the PMTs due to radioactivity of the glass

A full chain of simulations was performed to find the rates of these backgrounds for a representative set of detector sizes up to 50×50 . Secular equilibrium was assumed between the concentrations of U/Th and the resultant daughter decays. In RAT-PAC, the full U/Th decay chains are included. The assumed radiopurities for water and PMT glass are listed in Table VI. The PMT values were obtained from measurements of Hamamatsu R7081 PMTs. The water values were chosen to be consistent with previous water-based experiments such as SNO [38] and Super-K [14, 34].

Medium	^{238}U	^{232}Th	^{40}K	^{222}Rn
Water [Bq/kg]	1.0e-6	1.0e-7	4.0e-6	1.0e-6
PMT [Bq/PMT]	2.45e3	2.49e3	5.85e-1	—

TABLE VI. Radiopurity levels used in the calculations.

The detectors considered here were assumed to be placed at a depth roughly consistent with the proposed depth of the WATCHMAN experiment in the Boubou mine (~ 2.8 km water equivalent). At this depth, and assuming the detector fiducial volumes are protected by 4 meters of veto and PMT buffer as described above, cosmogenic fast-neutron backgrounds are expected to be subdominant. Muons when interacting with the detector medium can create long-lived isotopes (e.g. ^8He and ^9Li), that can potentially look like IBD events. At the Boubou depth, these can be effectively vetoed with minimal loss in livetime.

The rate of fast neutrons originating from muons interacting with the surrounding rock material was estimated using the Mei-Hime model [39]. A FLUKA simulation was performed to determine the rate and positions of neutron captures inside the 20×20 detector, and then scaled as the fiducial area. We estimate the rate of di-neutron events (that could mimic the IBD) as follows:

$$M_i = \sum_j A_{ij} P_j \quad (5)$$

$$A_{ij} = \epsilon^i (1 - \epsilon)^{j-i} \binom{j}{i} \quad (6)$$

where M_i — measured multiplicity (to detect two neutrons, $i = 2$), P_j — produced multiplicity (to produce j neutrons), $\binom{j}{i} = \frac{j!}{i!(j-i)!}$ is the binomial coefficient, and ϵ is the detection efficiency taken from Fig. 8 (a mean value is chosen corresponding to optimal n9 values for prompt and delayed).

The rates of exotic backgrounds such as from diffuse relic supernova antineutrinos and atmospheric neutrino-induced neutral-current interactions are unknown, though they are constrained to be small [23, 40, 41]. As such, these were estimated as follows: 4 events/10kt/yr (atmospheric neutrinos scatter off oxygen nuclei) and 2 events/10kt/yr (diffuse supernova relic antineutrinos). The uncertainties on these two types of backgrounds are expected to be significantly smaller in the near future, as the SuperK-Gd will likely measure them within the next couple of years.

In principle, the requirement that IBD event pairs be reconstructed within 2 meters places a significant limitation on the number of uncorrelated detector background events that result in an IBD-like event (see Fig. 9). The fraction of events that pass this criterion was calculated from simulation for a selection of representative detector sizes and plotted as a function of n9 cut. The results are presented in Fig. 10. The expectation was that for each detector size this fraction would be independent of the n9 cut. However, for larger detector sizes 40×40 and 50×50 , it appears that these two parameters are not independent. The reason appears to be for large detectors, there are a significant number of PMT hits caused by the PMT dark rate (see Figs. 10 and 11). These dark-rate-induced PMT events severely impact event reconstruction, causing many low n9 events to be pushed towards the center of the detector. While dark rate appears to be the cause, the effect can be removed by applying a higher n9 analysis cut (see Table V). For the 50×50 geometry, an optimal n9 cut was chosen 26 to eliminate the effect of the PMT dark rate. To determine the minimum n9 analysis cut, we calculate the ratio of the 2-meter volume divided by the fiducial volume. When the n9 cut applied in the simulation results in an equivalent 2-meter fraction (within uncertainty), it was assumed sufficient to correct for the effect.

For extremely large detector geometries, such as those greater than 50×50 , the PMT dark rate of 3 kHz begins to impact the vertex reconstruction algorithm. The effect could be seen in Fig. 5 and Fig. 10. For these detectors, either new ways must be found to reduce PMT dark rates, or larger-diameter PMTs should be used. The high dark rate affect the reconstruction algorithm. For large detectors, events start to reconstruct at the center of the detector, as demonstrated in Fig. 11.

A scan over n9 values was performed to determine the optimal n9 threshold cut for our set of representative detector sizes (shown in Fig. 6). The optimization parame-

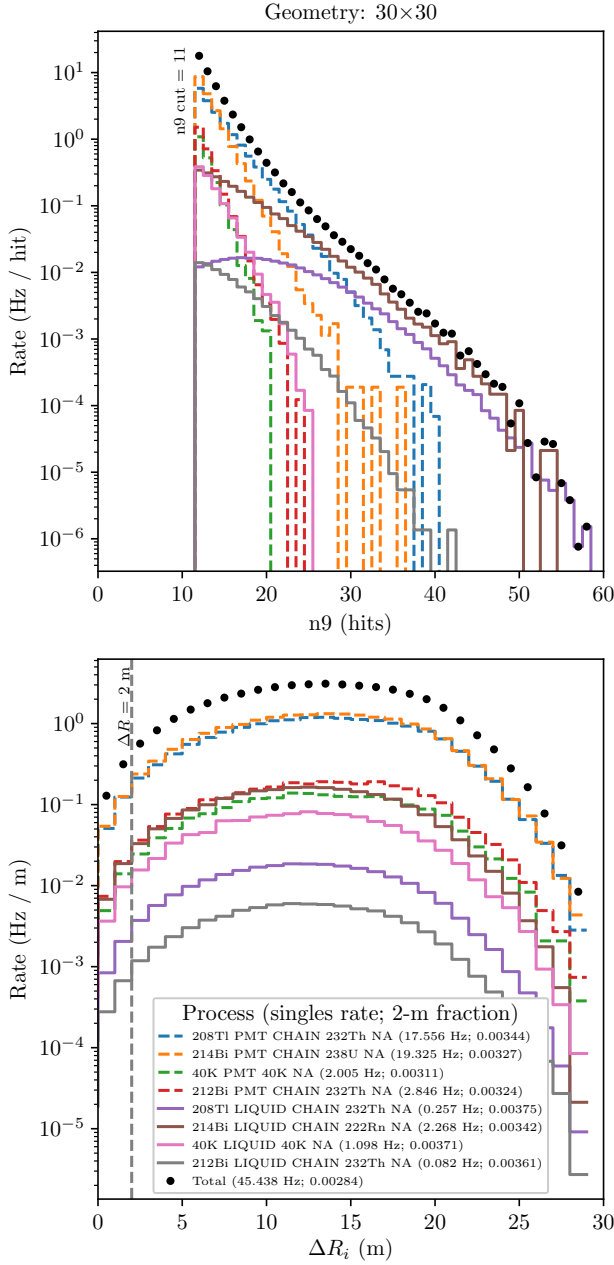


FIG. 9. Uncorrelated detector background (singles rate) inside the fiducial volume as a function of the n9 parameter for 30×30 geometry. The primary contributing processes in the PMTs and water are shown. *Bottom panel:* Also for a 30×30 detector, an example distribution (for an n9 cut of 11) of the distance between any two consecutive uncorrelated detector background events that reconstruct inside the fiducial volume. A line is drawn at the 2-m distance cut. The legend is shared between the two plots.

ter was the signal divided by the square root of the signal plus background. Only detector backgrounds were used since the cuts were chosen to optimally remove detector backgrounds while maximizing the reactor antineutrino

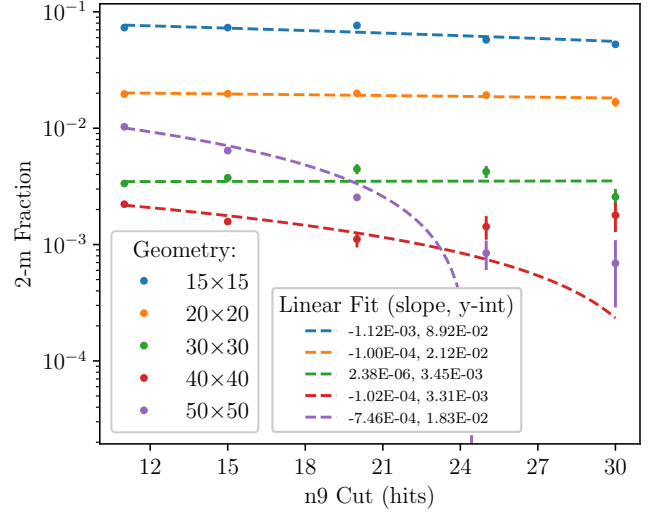


FIG. 10. Fraction of detector-induced accidental backgrounds events within a 2-m volume as a function of n9 cut for different geometries. Error bars are calculated as follows $\delta f = 1/\sqrt{\sum N_i R_i / R_{tot}}$, where N_i is a number of events within a 2-meter distance of each other; R_i — rate of i -th process; R_{tot} — total rate (after applying fiducial-volume and n9 cuts).

signal. The optimal n9 thresholds for any general detector size were determined by interpolation from these results.

RESULTS AND DISCUSSION

We use the Currie equation [42, 43] to evaluate the number of signal events required to register a significant detection. The Currie equation can be generalized to the total uncertainty on the background, including the statistical and systematic uncertainty as follows:

$$N_D = 4.653\sigma_B + 2.706 \quad (7)$$

The total uncertainty σ_B has statistical and systematic uncertainties added in quadrature:

$$\sigma_B^2 = \sigma_{stat}^2 + \sigma_{sys}^2 = N_B + (N_B\delta)^2 \quad (8)$$

and so,

$$N_D = 4.653\sqrt{N_B}\sqrt{1 + N_B\delta^2} + 2.706 \quad (9)$$

where N_D is the minimum number of counts from the source (antineutrinos from a 50-MW reactor) required to ensure a reliable detection in the presence of background — N_B is the total background, including world reactors, uncorrelated detector backgrounds, cosmogenic fast neutrons, atmospheric neutrino interactions on oxygen, diffuse supernova antineutrinos and geological antineutrinos. We assume that systematic uncertainty δ

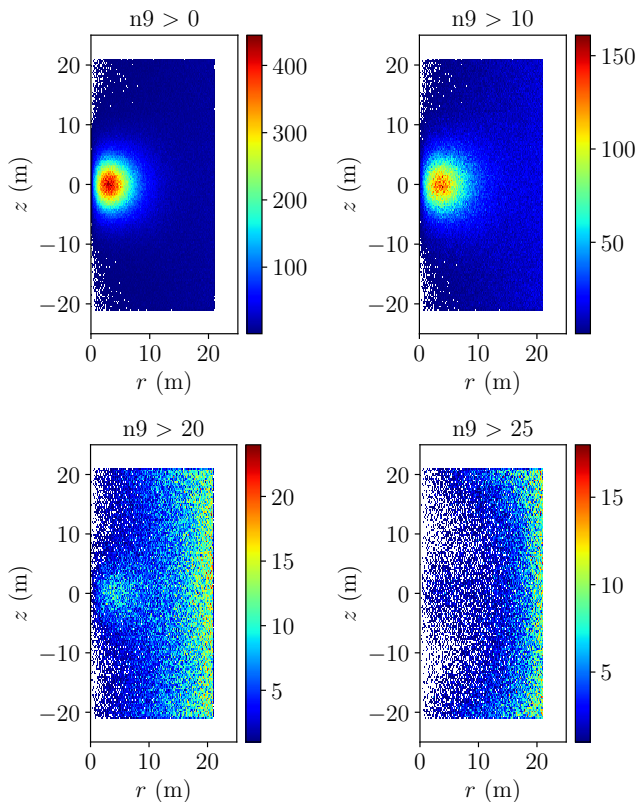


FIG. 11. Spatial distributions of events originating in water due to ^{208}Tl decays in the 50×50 detector (reconstructed position z vs $r = \sqrt{x^2 + y^2}$). The events that reconstruct in the middle of the detector (*top panel*) are due to the high PMT dark rate affecting the reconstruction algorithm. If the value for $n9$ cut is increased, the reconstruction works better.

is symmetric, ensuring that the underlining assumptions used to derive the Currie equation remain valid (i.e. systematic and statistical uncertainties added in quadrature and the total systematic uncertainty remains Gaussian). For low-count circumstances such as for short dwell times or long base-lines, systematic uncertainty δ can have an important impact on N_D . The dwell time as a function of distance and the effect of adding non-zero systematic uncertainties ($\delta = 2\%$, 5% , and 10%) are shown in Fig. 12.

The flux and spectrum of reactor antineutrinos for any reactor-detector distance was calculated by applying the up-to-date neutrino-oscillation parameters as shown in Fig. 1. Since the world-wide reactor flux background can vary considerably depending on where in the world the detector is placed, three locations were chosen as broadly representative of three reactor background cases: high, medium and low. The three locations chosen were Andes, Baksan, and Frejus underground laboratories. The web tool, geoneutrinos.org, was used to calculate the world-reactor antineutrino fluxes in those locations [44]. Unlike detector backgrounds, antineutrino backgrounds cannot

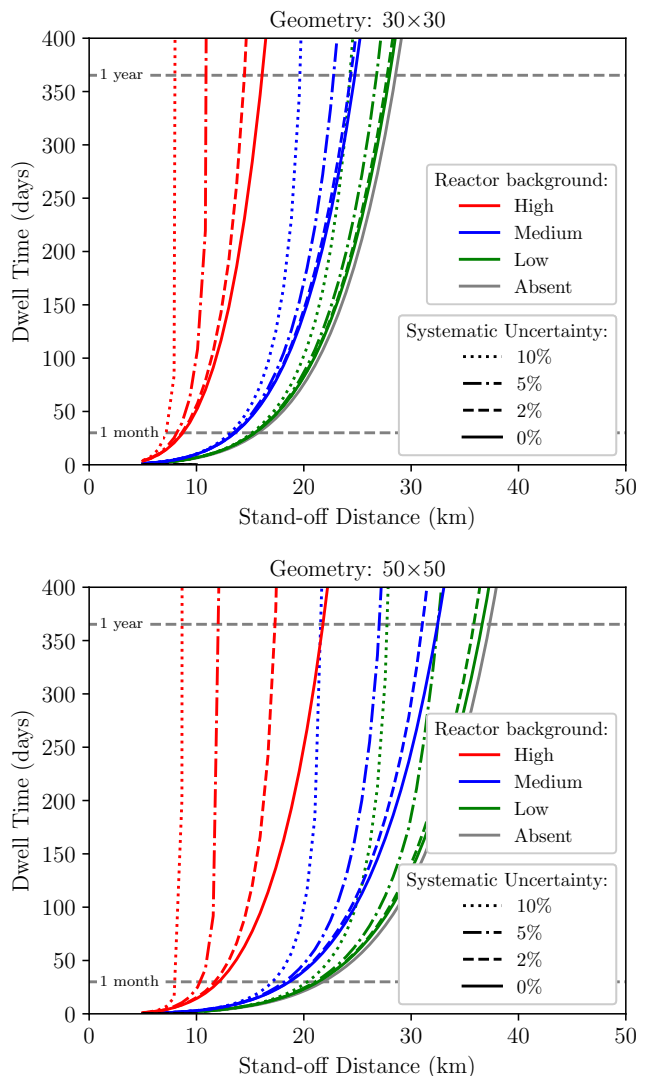


FIG. 12. Dwell time for two different geometries (30×30 and 50×50) as a function of stand-off distance to the 50-MWt reactor. The color represents world-reactor backgrounds. The line style represents four different levels of systematic uncertainties (0%, 2%, 5%, and 10%), based on Eq. 9. For clarity, the systematic effects are not shown for the “absent” world-reactor-background curve. The Gaussian assumption remains valid for dwell times greater than approximately one month. For smaller dwell times, a Poisson treatment is more accurate.

be removed by applying clever analysis cuts, and so the world’s reactors comprise an important and irreducible background in these calculations.

Other important performance parameters needed for this analysis were the detector background rates as a function of $n9$ (energy) (Fig. 9), and the fraction of uncorrelated detector backgrounds that reconstruct inside the fiducial volume and within the 2-m proximity requirement for IBD events. Fig. 9 also shows the distribution of uncorrelated detector backgrounds as a function of the distance from previous event for a variety of different de-

Detector		Signal (50-MWt)			Backgrounds						
D×H	m_{fid}/kt	10-km	20-km	50-km	World-Reactor			Accidental	Cosmogenic	Exotic	Geo
					Low	Med.	High				
20×20	1.3	89	20	2	2	19	248	2	24	1	<1
30×30	8.4	498	113	9	11	105	1388	7	81	5	2
40×40	25.7	1232	280	23	26	258	3397	17	165	15	3
50×50	58.2	1614	372	34	33	324	4017	2	247	35	3

TABLE VII. Number of counts per year for signal and various backgrounds in the simulated detector geometries. The signal annual rates are reported for 10, 20, and 50-km baselines.

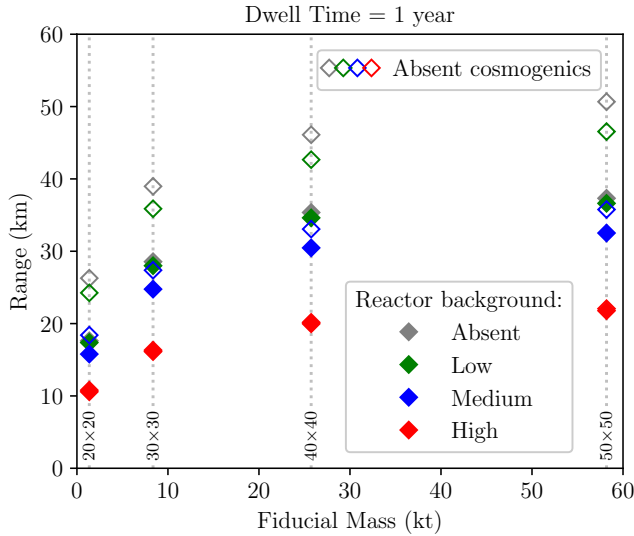


FIG. 13. Range as a function of stand-off distance for a 1-year dwell time at the three world-reactor backgrounds. The empty rhombi indicate scenarios with zero cosmogenic fast-neutron backgrounds.

tector backgrounds.

For high world-reactor background locations (e.g. the Frejus site at the border between France and Italy), the task of detecting a small 50-MWt reactor at a large distance depends primarily on the world-reactor background at that location. This is the primary reason why the estimated range levels off as a function of detector size in Fig. 13.

All other backgrounds, such as those associated with detector radiopurity and cosmogenic interactions were found to be subdominant for the Frejus location. Although geological antineutrinos were included in the calculations, they were easily rejected, as their energies were either below the detection threshold, or not far enough above it to produce an energetic enough event for detection. Table VII shows the number of signal and background events for each detector location. The signal values presented in Table VII were calculated using Eq. 3, where the positron, neutron, spatial, and temporal efficiencies were based on Fig. 3, Fig. 8, and Table V.

One significant outcome of this work is that it is clear

that water-Cherenkov detectors, despite the clarity of the detection medium, seem to approach a sensitivity limit at the 50×50 scale (as shown in Fig. 13). Detectors at this scale appear to level off in sensitivity at ~50 km due to a combination of neutrino oscillations, which become significant at that distance, PMT dark rate, and detector self absorption, which appears to impact performance at the 50×50 scale. The problem of the negative effect of PMT dark rate on event reconstruction severely impacts sensitivity in this work. However, improvements in event reconstruction algorithms might be able to overcome this difficulty [45]. Such improvements, if achievable, were considered outside the scope of this work.

ACKNOWLEDGEMENTS

This work is supported by the U.S. Department of Energy National Nuclear Security Administration and Lawrence Livermore National Laboratory [Contract No. DE-AC52-07NA27344, release number LLNL-JRNL-823255]. We thank the WATCHMAN collaboration for useful comments and critique at various stages of this study. In particular, we thank Felicia Sutanto for performing the FLUKA fast-neutron simulation. V.L. thanks Mark Duvall for the help with visualization of large geometries in RAT-PAC. All computations were performed on the Livermore-Computing Lassen cluster running Red Hat Linux operating system. Analysis routines were written using ROOT 6 [46] and Python 3, primarily with NumPy [47], SciPy [48], Pandas [49], and Matplotlib [50] packages.

* corresponding author: li68@llnl.gov

- [1] A. A. Borovoi and L. A. Mikaelyan, “Possibilities of the practical use of neutrinos,” *Soviet Atomic Energy* **44**, 589–592 (1978).
- [2] E. Fermi, “An attempt of a theory of beta radiation,” *Z. Phys.* **88**, 161–177 (1934).
- [3] S. E. Bays, G. A. Reyes, M. J. Schanfein, R. H. Stewart, and N. P. Martin, “Significant Quantity Production Rates in Small Modular Reactors,” *Proceedings of*

- the INMM and ESARDA Joint Virtual Annual Meeting (2021).
- [4] C. L. Cowan, F. Reines, F. B. Harrison, H. W. Kruse, and A. D. McGuire, “**Detection of the free neutrino: A Confirmation**,” *Science* **124**, 103–104 (1956).
 - [5] F. Boehm, J. Busenitz, B. Cook, G. Gratta, H. Henriksen, J. Kornis, D. Lawrence, K. B. Lee, K. McKinny, L. Miller, *et al.* (Palo Verde), “**Search for neutrino oscillations at the Palo Verde nuclear reactors**,” *Phys. Rev. Lett.* **84**, 3764–3767 (2000).
 - [6] M. Apollonio, A. Baldini, C. Bemporad, E. Caffau, F. Ceci, Y. Déclais, H. de Kerret, B. Dieterle, A. Etenko, L. Foresti, *et al.* (CHOOZ), “**Search for neutrino oscillations on a long baseline at the CHOOZ nuclear power station**,” *Eur. Phys. J.* **C27**, 331–374 (2003).
 - [7] Y. Abe, C. Aberle, T. Akiri, J. C. dos Anjos, F. Ardellier, A. F. Barbosa, A. Baxter, M. Bergevin, A. Bernstein, T. J. C. Bezerra, *et al.* (Double Chooz), “**Indication of Reactor $\bar{\nu}_e$ Disappearance in the Double Chooz Experiment**,” *Phys. Rev. Lett.* **108**, 131801 (2012).
 - [8] F. P. An, J. Z. Bai, A. B. Balantekin, H. R. Band, D. Beavis, W. Beriguete, M. Bishai, S. Blyth, K. Boddy, R. L. Brown, *et al.* (Daya Bay), “**Observation of electron-antineutrino disappearance at Daya Bay**,” *Phys. Rev. Lett.* **108**, 171803 (2012).
 - [9] J. K. Ahn, S. Chebotaryov, J. H. Choi, S. Choi, W. Choi, Y. Choi, H. I. Jang, J. S. Jang, E. J. Jeon, I. S. Jeong, *et al.* (RENO), “**Observation of Reactor Electron Antineutrino Disappearance in the RENO Experiment**,” *Phys. Rev. Lett.* **108**, 191802 (2012).
 - [10] T. Araki, K. Eguchi, S. Enomoto, K. Furuno, K. Ichimura, H. Ikeda, K. Inoue, K. Ishihara, T. Iwamoto, T. Kawashima, *et al.* (KamLAND), “**Measurement of neutrino oscillation with KamLAND: Evidence of spectral distortion**,” *Phys. Rev. Lett.* **94**, 081801 (2005).
 - [11] F. An, G. An, Q. An, V. Antonelli, E. Baussan, J. Beacom, L. Bezrukov, S. Blyth, R. Brugnera, M. Buizza Avanzini, *et al.* (JUNO), “**Neutrino Physics with JUNO**,” *J. Phys. G* **43**, 030401 (2016).
 - [12] M. Baldoncini, V. Strati, S. A. Wipperfurth, G. Fiorentini, F. Mantovani, W. F. McDonough, and B. Ricci, “**Geoneutrinos and reactor antineutrinos at SNO+**,” *J. Phys. Conf. Ser.* **718**, 062003 (2016).
 - [13] K. C. Abe, C. Bronner, Y. Hayato, K. Hiraide, M. Ikeda, S. Imaizumi, J. Kameda, Y. Kanemura, Y. Kataoka, S. Miki, *et al.* (Super-Kamiokande), “**First gadolinium loading to Super-Kamiokande**,” *Nucl. Instrum. Meth. A* **1027**, 166248 (2022).
 - [14] L. Marti, M. Ikeda, Y. Kato, Y. Kishimoto, M. Nakahata, Y. Nakajima, Y. Nakano, S. Nakayama, Y. Okajima, A. Orii, *et al.*, “**Evaluation of gadolinium’s action on water Cherenkov detector systems with EGADS**,” *Nucl. Instrum. Meth. A* **959**, 163549 (2020).
 - [15] M. Askins, M. Bergevin, A. Bernstein, S. Dazeley, S. T. Dye, T. Handler, A. Hatzikoutelis, D. Hellfeld, P. Jaffke, Y. Kamyshkov, *et al.* (WATCHMAN), “**The Physics and Nuclear Nonproliferation Goals of WATCHMAN: A Water Cherenkov Monitor for Antineutrinos**,” arXiv:1502.01132 (2015).
 - [16] P. A. Cherenkov, “**Visible luminescence of pure liquids under the influence of gamma-radiation**,” *Dokl. Akad. Nauk SSSR* **2**, 451–454 (1934), [*Usp. Fiz. Nauk* 93, 385 (1967)].
 - [17] I. M. Frank and I. E. Tamm, “**Coherent visible radiation of fast electrons passing through matter**,” *Dokl. Akad. Nauk SSSR* **14**, 109–114 (1937), [*Usp. Fiz. Nauk* 93, 388 (1967)].
 - [18] K. Hagiwara, T. Yano, T. Tanaka, M. S. Reen, P. K. Das, S. Lorenz, I. Ou, T. Sudo, Y. Yamada, T. Mori, *et al.*, “**Gamma Ray Spectrum from Thermal Neutron Capture on Gadolinium-157**,” *PTEP*, 023D01 (2019).
 - [19] T. Tanaka, K. Hagiwara, E. Gazzola, A. Ali, I. Ou, T. Sudo, P. K. Das, M. S. Reen, R. Dhir, Y. Koshio, *et al.*, “**Gamma Ray Spectra from Thermal Neutron Capture on Gadolinium-155 and Natural Gadolinium**,” *PTEP*, 043D02 (2020).
 - [20] R. M. Pope and E. S. Fry, “**Absorption spectrum (380–700 nm) of pure water. II. Integrating cavity measurements**,” *Appl. Opt.* **36**, 8710–8723 (1997).
 - [21] K. Abe, Y. Hayato, T. Iida, K. Iyogi, J. Kameda, Y. Kishimoto, Y. Koshio, L. Marti, M. Miura, S. Moriyama, *et al.*, “**Calibration of the Super-Kamiokande Detector**,” *Nucl. Instrum. Meth. A* **737**, 253–272 (2014).
 - [22] A. Bernstein, T. West, and V. Gupta, “**An assessment of antineutrino detection as a tool for monitoring nuclear explosions**,” *Science & Global Security* **9**, 235–255 (2001).
 - [23] J. F. Beacom and M. R. Vagins, “**Anti-neutrino spectroscopy with large water Cherenkov detectors**,” *Phys. Rev. Lett.* **93**, 171101 (2004).
 - [24] H. Watanabe, H. Zhang, K. Abe, Y. Hayato, T. Iida, M. Ikeda, J. Kameda, K. Kobayashi, Y. Koshio, M. Miura, *et al.*, “**First study of neutron tagging with a water Cherenkov detector**,” *Astroparticle Physics* **31**, 320–328 (2009).
 - [25] S. Dazeley, A. Asghari, A. Bernstein, N. S. Bowden, and V. Mozin, “**A water-based neutron detector as a well multiplicity counter**,” *Nucl. Instrum. Meth. A* **771**, 32–38 (2015).
 - [26] H. P. Lima Jr., J. A. M. Alfonzo, J. C. Anjos, G. Cernicchiaro, P. Chimenti, I. A. Costa, M. P. Dias, P. C. M. A. Farias, A. Fernandes Jr., G. P. Guedes, *et al.*, “**Neutrinos Angra experiment: commissioning and first operational measurements**,” *Journal of Instrumentation* **14**, 06010 (2019).
 - [27] S. Dazeley, M. Askins, M. Bergevin, A. Bernstein, N. S. Bowden, T. M. Shokair, P. Jaffke, S. D. Rountree, and M. Sweany, “**A search for cosmogenic production of beta-neutron emitting radionuclides in water**,” *Nucl. Instrum. Meth. A* **821**, 151–159 (2016).
 - [28] A. R. Back, J. F. Beacom, M. Bergevin, E. Catano-Mur, S. Dazeley, E. Drakopoulou, F. Di Lodovico, A. Elagin, J. Eisch, V. Fischer, *et al.* (ANNIE), “**Accelerator Neutrino Neutron Interaction Experiment (ANNIE)**,” arXiv:1707.08222 (2017).
 - [29] A. Strumia and F. Vissani, “**Precise quasielastic neutrino-nucleon cross-section**,” *Phys. Lett.* **B564**, 42–54 (2003).
 - [30] P. Huber, “**On the determination of anti-neutrino spectra from nuclear reactors**,” *Phys. Rev. C* **84**, 024617 (2011).
 - [31] A. Bernstein, N. Bowden, B. L. Goldblum, P. Huber, I. Jovanovic, and J. Mattingly, “**Colloquium: Neutrino detectors as tools for nuclear security**,” *Rev. Mod. Phys.* **92**, 011003 (2020).
 - [32] M. Smy (Super-Kamiokande), “**Low Energy Event Reconstruction and Selection in Super-Kamiokande-III**,” Proceedings of the 30th International Cosmic Ray Con-

- ference , 1279–1282 (2007).
- [33] T. Tomura, Y. Hayato, M. Ikeno, M. Nakahata, S. Nakayama, Y. Obayashi, K. Okumura, M. Shiozawa, S. Y. Suzuki, T. Uchida, *et al.*, “[Development of New Data Acquisition System at Super-Kamiokande for Nearby Supernova Bursts](#),” *IEEE Transactions on Nuclear Science* **60**, 3694–3697 (2013).
- [34] K. Abe, Y. Haga, Y. Hayato, M. Ikeda, K. Iyogi, J. Kameda, Y. Kishimoto, L. Marti, M. Miura, S. Moriyama, *et al.* (Super-Kamiokande), “[Solar Neutrino Measurements in Super-Kamiokande-IV](#),” *Phys. Rev. D* **94**, 052010 (2016).
- [35] S. Seibert, T. Bolton, D. Gastler, J. Klein, H. Lippincott, A. Mastbaum, J. Nikkel, G. Orebi Gann, M. Akashi-Ronquest, S. Sekula, *et al.*, “[RAT-PAC analysis package](#),” online documentation (accessed 2022).
- [36] S. Agostinelli, J. Allison, K. Amako, J. Apostolakis, H. Araujo, P. Arce, M. Asai, D. Axen, S. Banerjee, G. Barrand, *et al.* (GEANT4), “[GEANT4: A Simulation toolkit](#),” *Nucl. Instrum. Meth. A* **506**, 250–303 (2003).
- [37] Y. Nakano, T. Hokama, M. Matsubara, M. Miwa, M. Nakahata, T. Nakamura, H. Sekiya, Y. Takeuchi, S. Tasaka, and R.A. Wendell, “[Measurement of the radon concentration in purified water in the Super-Kamiokande IV detector](#),” *Nucl. Instrum. Meth. A* **977**, 164297 (2020).
- [38] N. Jolley, A. B. McDonald, and R. G. Hamish Robertson, “[The Sudbury Neutrino Observatory](#),” *Ann. Rev. Nucl. Part. Sci.* **59**, 431–465 (2009).
- [39] D. Mei and A. Hime, “[Muon-induced background study for underground laboratories](#),” *Phys. Rev. D* **73**, 053004 (2006).
- [40] M. Leyton and S. Dye, “[Prospects for long-range reactor monitoring with gadolinium-loaded water-Cherenkov detectors](#),” *Proceedings of the 13th International Workshop on Applied Antineutrino Physics* (2017).
- [41] L. Wan, K. Abe, C. Bronner, Y. Hayato, M. Ikeda, K. Iyogi, J. Kameda, Y. Kato, Y. Kishimoto, L. Marti, *et al.* (Super-Kamiokande Collaboration), “[Measurement of the neutrino-oxygen neutral-current quasielastic cross section using atmospheric neutrinos at Super-Kamiokande](#),” *Phys. Rev. D* **99**, 032005 (2019).
- [42] L. A. Currie, “[Limits for qualitative detection and quantitative determination. Application to radiochemistry](#),” *Analytical Chemistry* **40**, 586–593 (1968).
- [43] G. Knoll, *Radiation Detection and Measurement (4th ed.)* (Wiley, 2010).
- [44] A. Barna and S. Dye, “[Global Antineutrino Modeling: A Web Application](#),” arXiv:1510.05633 (2015).
- [45] E. Kneale, *Coincidence-based reconstruction and analysis for remote reactor monitoring with antineutrinos*, Ph.D. thesis, University of Sheffield (2021).
- [46] R. Brun and F. Rademakers, “[ROOT: An object-oriented data analysis framework](#),” *Nucl. Instrum. Meth. A* **389**, 81–86 (1997).
- [47] C. R. Harris, K. J. Millman, S. J. van der Walt, R. Gommers, P. Virtanen, D. Cournapeau, E. Wieser, J. Taylor, S. Berg, N. J. Smith, *et al.*, “[Array programming with NumPy](#),” *Nature* **585**, 357–362 (2020).
- [48] P. Virtanen, R. Gommers, T. E. Oliphant, M. Haberland, T. Reddy, D. Cournapeau, E. Burovski, P. Peterson, W. Weckesser, J. Bright, *et al.*, “[SciPy 1.0—Fundamental Algorithms for Scientific Computing in Python](#),” *Nature Meth.* **17**, 261 (2020).
- [49] W. McKinney, “[Data Structures for Statistical Computing in Python](#),” *Proceedings of the 9th Python in Science Conference* , 56–61 (2010).
- [50] J. D. Hunter, “[Matplotlib: A 2D graphics environment](#),” *Computing in Science & Engineering* **9**, 90–95 (2007).